https://dx.doi.org/10.1016/j.joule.2022.06.009

Aperiodic Band-Pass Electrode enables Record-performance Transparent Organic Photovoltaics

Xin Liu[1], Ziping Zhong[1], Rihong Zhu[1], Jiangsheng Yu[1,2*], and Gang Li[2,3*]

[1]MIIT Key Laboratory of Advanced Solid Laser, School of Electronic and Optical Engineering, Nanjing University of Science and Technology, Nanjing 210094, China

[2]Department of Electronic and Information Engineering, Research Institute for Smart Energy (RISE), The Hong Kong Polytechnic University, Hong Kong, China

[3]Lead Contact

*Correspondence:

yjs@njust.edu.cn (J.Y.),

gang.w.li@polyu.edu.hk (G.L.)

SUMMARY

Transparent organic photovoltaics (TOPVs) potentially meet the demands of building integration windows, while a critical challenge for highly efficient TOPVs is the trade-off between average visible light transmittance (AVT) and power conversion efficiency (PCE). Herein, we successfully design and construct a superior transparent rear electrode for efficient TOPVs via integrating an aperiodic band-pass filter (ABPF, aperiodic [lithium fluoride (LiF)/tellurium dioxide (TeO_2)]^8/ LiF). The versatile aperiodic band-pass rear electrode exhibits an AVT of up to 78.69% and color rendering index (CRI)

of 97.54, and total reflection in the near-infrared region (700-900 nm). Relative to the counterparts without ABPF, the TOPVs with ABPF demonstrated remarkable ~60% enhancement in AVT and light utilization efficiency (LUE). As a result, ABPF integrated TOPVs demonstrate a record-breaking LUE of 5.35%, accompanied with an AVT of 46.79% and CRI of 85.39. This superior transparent electrode realization - highly transparent in visible and total reflection in NIR represents a significant step forward towards unique and versatile TOPVs applications.

KEYWORDS

transparent organic photovoltaics; light utilization efficiency; transparent rear electrode; aperiodic band-pass filter; NIR non-fullerene acceptors

INTRODUCTION

Organic photovoltaics (OPVs) is regarded as an emerging green energy technology that combines the advantages of abundance of photoactive materials, freedom of form factor, and environmental friendliness.[1-5] Recently, opaque OPVs with power conversion efficiencies (PCEs) approaching 20% have been reported with the concerted efforts of engineering in photoactive materials and interfacial materials, and device engineering in the laboratory.[6,7] As organic semiconductor materials with more discrete absorption can be deliberately designed to focus light absorption in the ultra-violet (UV) and near-infrared (NIR) regions, and exhibit weak absorption in the visible range, OPVs is the most naturally suited photovoltaic technology for transparent devices. Transparent OPVs (TOPVs) can work as an auxiliary energy source to be integrated with windows, skylights, automobiles, greenhouses, and

large public spaces, providing a very precious entry point into the niche market of the photovoltaic field.[8-20] Therefore, it is strategically important to have dedicated research and development efforts on TOPVs.

Transparent photovoltaic devices aim at maximizing both the power conversion efficiency (PCE) and the average visible transmittance (AVT), hence the light utilization efficiency (LUE = PCE×AVT) has been proposed as an appropriate figure of merit to track the progress of transparent devices.[21] Other key factors to assess the performance of TOPVs include chromaticity coordinates (CIE1931) and color rendering index (CRI).[22,23] Despite the fact that numerous OPVs with PCEs exceeding 18% are sprouting up in the state-of-the-art, the LUE of related TOPVs are basically stalled with a value of less than 5%. To achieve high LUE for TOPVs, the involved active-layer materials should have strong absorption in the NIR and/or the UV region, and weak absorption in the visible region to ensure high current density values and high transparency in the visible region. The photovoltaic performance of TOPVs is also depended on transparent rear electrode. Various transparent rear electrodes have been developed, such as ultrathin metal[24-26], metal nanowires[27-32], conductive polymer (PH1000)[33,34], conductive oxide (ITO or AZO)[35], and graphene[36-38]. Among them, ultrathin metal films (10-20 nm), such as silver and gold, are extensively utilized as transparent rear electrode due to the flexibility and repeatability of vacuum evaporation process, and high-performance TOPVs.

Superior absorbing selectivity is the key for high-performance TOPVs, which should be taken into account for materials screen and device architecture design.[39-41] An ideal transparent rear electrode

should have high transmission in the visible range to enable a considerable AVT value of TOPVs. Meantime, total reflection in NIR region of the rear electrode is ideally desired for maximizing the photon harvesting in TOPV device, resulting in high J_{SC} and further PCE enhancement. Light management engineering provides a facile way to improve the optical property of ultrathin metal electrodes. A distributed Bragg reflector (DBR), as one common type of one-dimensional photonic crystals (1DPCs), is a structure formed from multiple layers of alternating materials with discrepant refractive indexes, owning the potential to manage the distribution of light intensity within the device.[42,43] In principle, photons in a DBR will be reflected when their energy is smaller than the bandgap of the photonic crystal, implying the selective bandpass of incident light. The intensity of optical reflection can be modulated by tuning the periodic pair number of the 1DPCs. Among the reported approaches of light management, the deposition of a periodic 1DPC on the top electrode can provide enhanced optical reflection in a selected wavelength range.[44-46] Nevertheless, the transmission curves of periodic 1DPCs exhibit non-uniform transmittance in the visible region due to the intense interference, which is fatal for the construction of uniform highly transparent electrodes. The current density reduction owing to the photon harvesting losses in the NIR range still dominates the dissatisfying performance of TOPVs. Along with the rapid development of NIR non-fullerene acceptors (NFAs, Y6, and its derivatives), it is critical to design a well-matched ideal transparent rear electrode to enable breakthrough in TOPVs.

In this work, a superior transparent rear electrode for efficient TOPVs has been deliberately designed

via integrating an aperiodic band-pass filter (ABPF, aperiodic (LiF/ TeO_2)^8 /LiF), and fabricated via thermal evaporation. Considering the non-uniform transmittance of ultra-thin silver film at different wavelengths and the representative NIR-absorbing high-performing NFAs (Y6 derivatives) with a narrow bandgap of about 1.35 eV, we construct the targeted transparent rear electrode with ABPF through alternating tellurium dioxide (TeO_2, high refractive index of 1.94015) and lithium fluoride (LiF, low refractive index of 1.31479) layers, where an optical forbidden bandwidth of 200 nm with a central wavelength of 800 nm is set up. Herein, the optical simulations by the Essential Macleod optical coating design program are validated through transfer matrix method (TMM), and the experimental results accord well with the simulations. Compared with the regular transparent rear electrode based on Glass/ PDINN/ Ag (12 nm), the targeted ABPF-based transparent rear electrode with a configuration of Glass/ PDINN/ Ag (12 nm)/ABPF exhibits outstanding optical properties with enhanced optical band-pass at 400-700 nm (i.e. visible) and an optical band-stop at 700-900 nm (i.e. NIR), delivering an AVT of 78.69% and a CRI of up to 97.54. An antireflection coating (ARC) integrated with glass substrate is designed with a configuration of (LiF/ TeO_2)^4, resulting in an enhancement of over 3.8% in AVT. Subsequently, the performance of TOPVs is systematically studied through tuning the ratio and thickness of PM6: BTP-eC9 bulk heterojunction (BHJ) films. A common ternary strategy of PM6: BTP-eC9: L8-BO is utilized to further boost the photovoltaic performance. Compared with the counterparts of binary PM6: BTP-eC9 based devices, ternary device exhibits improved PCE from higher short-circuit current density (J_{SC}) and open-circuit voltage (V_{OC}). The pristine TOPVs device

fabricated with an optimal ratio of PM6: BTP-eC9: L8-BO (0.8: 1: 0.2) and 75-nm BHJ film exhibited a high LUE of 3.31%, accompanied with an AVT of 29.71% and a PCE of 11.15%. Astoundingly, a recorded LUE of 5.35% accompanied with an AVT of 46.79% and a PCE of 11.44% is achieved with the architecture of (LiF/ TeO_2)^4/ Glass/ ITO/ PEDOT: PSS/ PM6: BTP-eC9: L8-BO (0.8:1:0.2)/ PDINN/ Ag (12 nm)/ (LiF/ TeO_2)^8/ LiF in devices. The corresponding TOPVs with ABPF demonstrate ~60% enhancement in AVT and LUE with slight enhancement in PCE, which is attributed to the enhanced visible transmittance and total reflection in the NIR region (700-900 nm). To our best knowledge, the LUE of 5.35% as the figure of merit for single-junction TOPVs is the highest value in the literature. This optical design of aperiodic band-pass electrode can be universally applied to improve AVT and LUE in high-efficiency transparent devices, accelerating the commercialization of TOPVs.

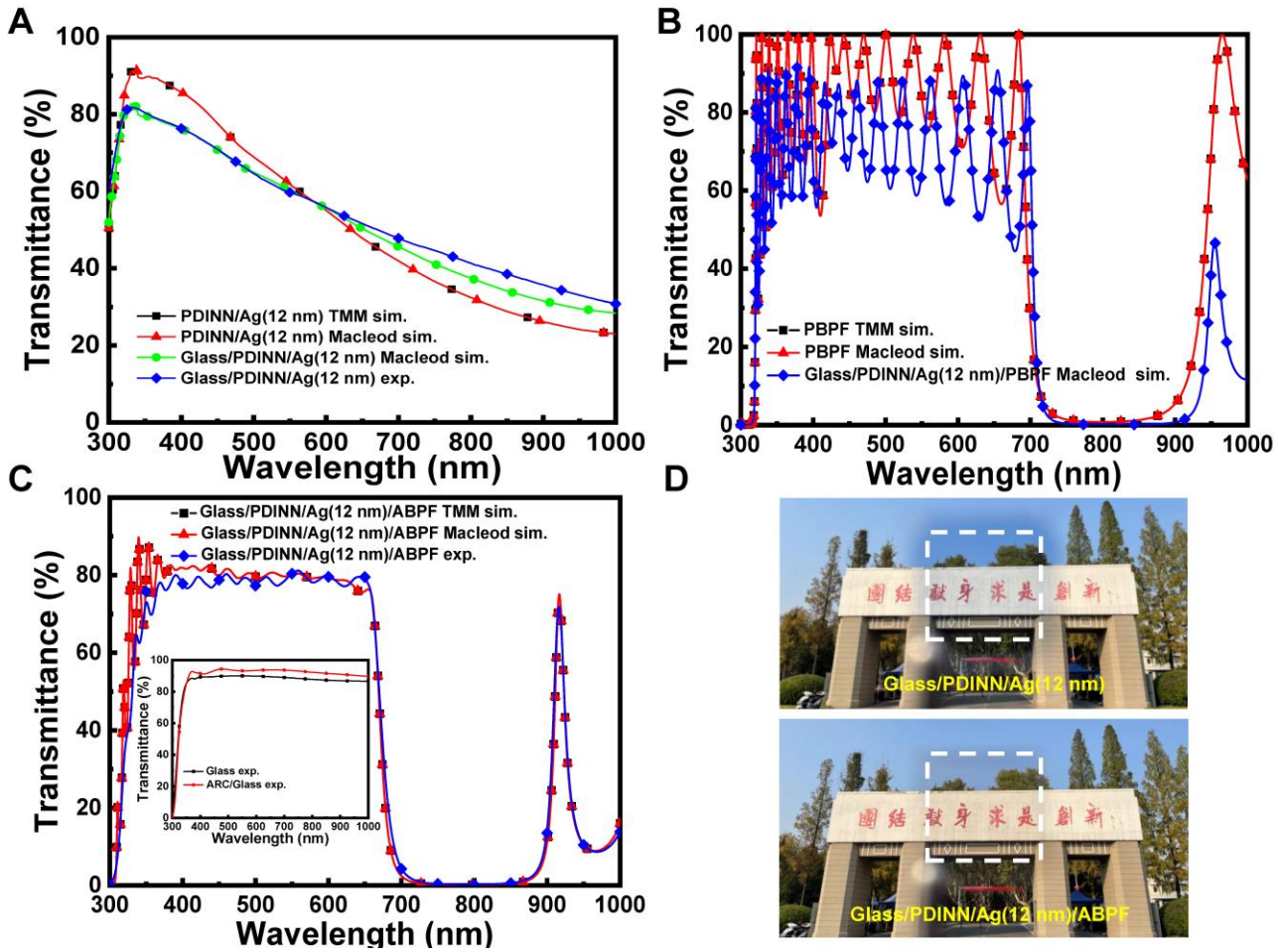

Figure 1. The design of ABPF integrated transparent electrode

(A) The simulated and experimental transmittance curves of PDINN/ Ag (12 nm) and Glass/ PDINN/ Ag (12 nm) films through TMM and Macleod methods

(B) The simulated transmittance curves of PBPF and Glass/ PDINN/ Ag (12 nm)/ PBPF films

(C) The simulated transmittance curves of Glass/ PDINN/ Ag (12 nm)/ ABPF ($[LiF/ TeO_2]^8$/ LiF), the experimental transmittance curves of Glass and ARC/ Glass (Inside).

(D) Photographs of Glass/ PDINN/ Ag (12 nm) and ARC/ Glass/ PDINN/ Ag (12 nm)/ ABPF with Nanjing University of Science and Technology landmark as background.

RESULTS AND DISCUSSION

An optical model based on the TMM is established for investigating the optical interference effect of multilayers in solar cells. The thickness of thin Ag film is set at 12 nm to account for its conductivity

and transmittance.[47] Firstly, the transmission curve of PDINN/ Ag (12 nm) was simultaneously simulated through the TMM and Essential Macleod optical coating design program. Each composing layer used in this work is represented by its complex refractive indices ($\tilde{n}(\lambda) = n(\lambda) + ik(\lambda)$) acquired by the spectral ellipsometry technique as shown in **Figure S**1 in the supporting information. As shown in **Figure 1**A, the simulated results from both methods are exactly the same, indicating the reliability of Essential Macleod optical coating design program for solar cells. The transmittance of an experimental substrate of Glass/ PDINN/ 12-nm Ag is gradually decreased from 350 nm to 1000 nm accompanied with an AVT of 59.08% and a CRI of 85.96 (**Table S**1), which is consistent with the calculation.

The designed band-pass filters atop transparent electrodes are following the working principle of $\eta_H d_H = \eta_L d_L = \lambda_0/4$, where λ_0 is the center wavelength of the forbidden band, η and d represent the refractive index and thickness of optical material, respectively. Herein, two thermally evaporable materials, LiF (η_L of 1.31479) and TeO_2 (η_H of 1.94015) are utilized to construct the targeted band-pass filters. Considering the visible edge of 700nm, λ_0 was set at 800 nm owing to the bandgap of high-performing active layers (Y6 derivatives, about 1.35 eV). The transmission of periodic band-pass filters (PBPF) with the structure of (152.12-nm LiF/ 103.08-nm TeO_2)^8 was simulated as shown in **Figure 1**B (**Table S**2). The PBPF presents a concussive decline in the visible region with an AVT of 86.28%. Correspondingly, the integrated Glass/ PDINN/ 12-nm Ag/PBPF film exhibits a red-shifted optical stop band and a moderate AVT of 71.25%. To further optimize the properties of band-pass filter,

an aperiodic BPF (ABPF) was designed based on the optimization algorithm of the thin film design software (Essential Macleod). The systematic details of the thickness of each layer (LiF/ TeO_2) are summarized in **Table S**3. As shown in **Figure 1**C, the simulated ABPF presents a high AVT of 79.28% with a uniform transmittance in the visible region and almost total reflection in the NIR region (700-900 nm). And the ARC technology was also utilized to improve the transmittance of the glass substrate through altering LiF/ TeO_2 layers. The detailed parameters of ARC film in this work are shown in **Figure 1**C and summarized in **Table S**4. Notably, an enhancement of 3.87% in AVT can be achieved in the ARC/ Glass substrate. Consequently, the experimental multi-objective substrate of Glass/ PDINN/ Ag (12 nm)/ ABPF presents an AVT of 78.69% and a CRI of 97.54 with total reflection in the NIR region (700-900 nm), which is consistent with the calculation. To illustrate the transparent substrates from the perspective of the human eye, two images of Nanjing University of Science and Technology landmark were compared without and with ABPF (**Figure 1**D). This clearly indicates that the transparent rear electrode integrating ABPF can refer to an ideal transmittance and color rendering index. A scanning electron microscope (SEM) image of ABPF was measured as shown in **Figure 2**A. The smooth interface among LiF/ TeO_2 layers can be ascribed to the preparation method of thermal evaporation, which is also in favor of the accurate realization of optical calculation. We have fabricated the relative devices to test the parasitic absorption: Glass, ARC/Glass, Glass/ABPF, Glass/Ag, ARC/Glass/Ag, and Glass/Ag/ABPF, respectively. As shown in **Figure S2**, the parasitic absorption (1-T-R) of Glass, ARC/Glass, and Glass/ABPF structures is almost zero in the range of 300-1000 nm.

Due to the incorporation of Ag film, the parasitic absorption of Glass/Ag and ARC/Glass/Ag structure is almost unchanged, ~ 5% in the range of 400-1000 nm. The parasitic absorption of Glass/Ag/ABPF structure is also about 5% in the range of 400-650 nm, while increased (below 10%) in the 650-1000 nm range due to the combined effect of the Ag thin film and the optical interference caused by the multilayer stacked ABPF.

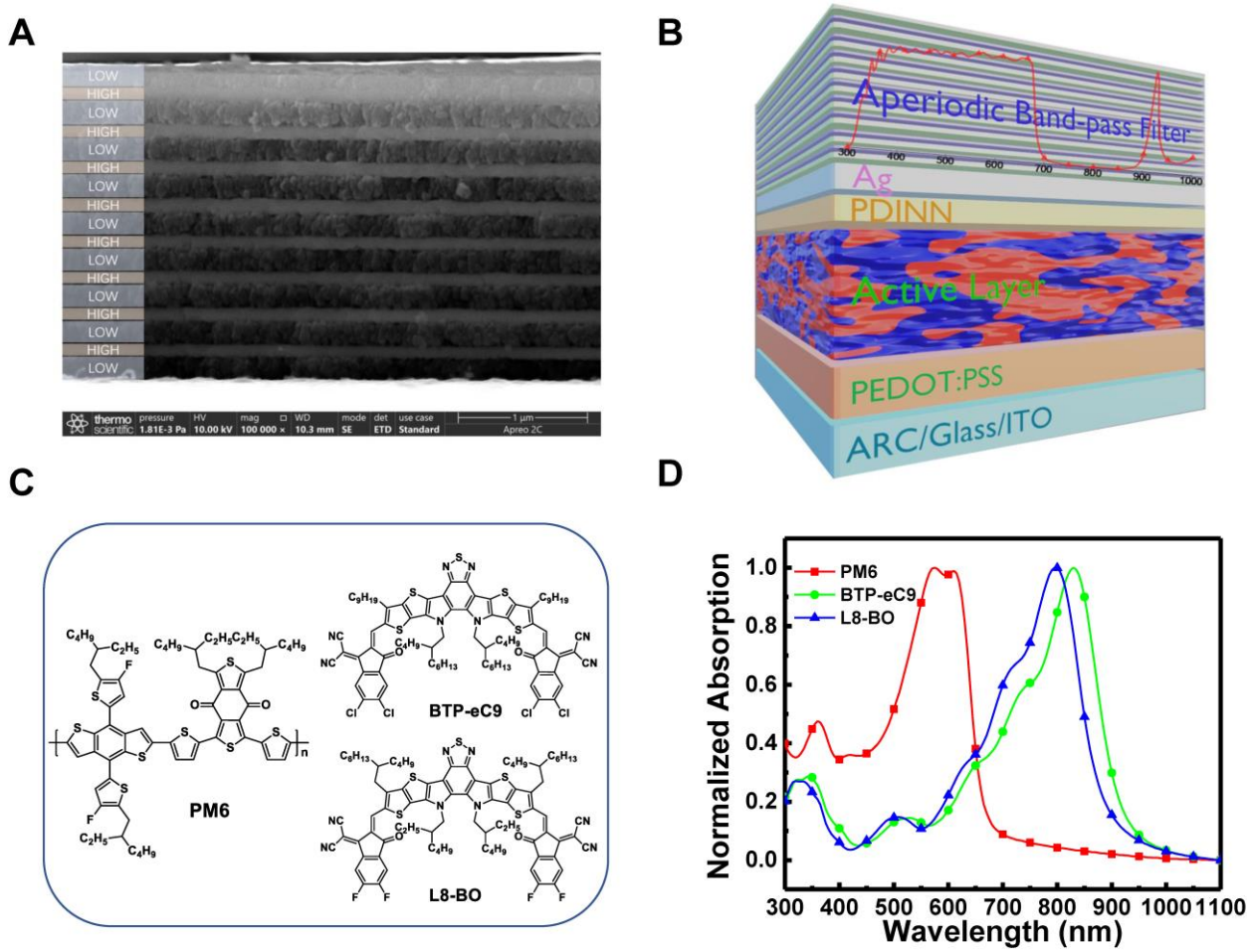

Figure 2. Chemical structures and the architecture of ABPF TOPVs

(A) Cross-sectional SEM measurement of the ABPF ([LiF/ TeO_2]^8/ LiF).

(B) The ABPF integrated TOPVs with an architecture of ARC/Glass/ ITO/ PEDOT: PSS/ Active Layer/ PDINN/ Ag /ABPF.

(C) Chemical structures of PM6, BTP-eC9, and L8-BO used in this work.

(D) Normalized film absorption of PM6, BTP-eC9, and L8-BO, respectively.

To explore the capacity of the ABPF based transparent rear electrode, TOPVs devices are fabricated with the conventional architectures of ARC/ Glass/ ITO (135 nm)/ PEDOT: PSS (30 nm)/ active layer /PDINN (10 nm)/ Ag (12nm)/ (with or without) ABPF (**Figure 2**B). The photovoltaic performance of relative devices are studied systematically through tuning the thicknesses, D: A ratios, and compositions of active layers. For the conventional devices, one donor material (PM6) and two acceptors (BTP-eC9 and L8-BO) are used for the active layer and their chemical structures are presented in **Figure 2**C. PM6 exhibits an absorption band vast majority in the visible region. Meanwhile, BTP-eC9 and L8-BO display broad absorption in the range of 600-930 nm (**Figure 2**D). The representative PM6: BTP-eC9 (weight ratio of 1: 1.2, opaque device optimized) as active layer was utilized firstly. A PCE of 17.81% for the opaque device was achieved as shown in **Figure S3**a and **Table S5**.

For the TOPVs with bare 12-nm Ag, the thicknesses (65-180 nm) of PM6: BTP-eC9 (1: 1.2) films are varied to tune the absorption and transmission of the devices (**Figure S**4). The related current density-voltage (*J-V*) curves, external quantum efficiency (EQE) curves, optical transmittance spectra (380-780nm), and the colored coordinates of the corresponding TOPVs were shown in **Figure S**5. The LUE value is gradually increased along with the decreased thickness of active layer. At the thickness (active layer) of 65 nm, the highest LUE of 2.66% is obtained accompanied with an AVT of 23.58%. The TOPV reaches a PCE of 11.26% with a J_{SC} of 17.46 mA cm^{-2}, an V_{OC} of 0.842 V, and a fill factor (FF) of 76.62%. (**Table S6**). The results indicated the reduction of active layer thickness was beneficial to

the LUE improvement for TOPVs. The D: A ratios were turned down to 0.8: 1.2 and 0.5: 1.2 due to the main visible absorption of PM6. For TOPVs (12-nm Ag) with a D: A ratio of 0.8: 1.2 (**Figure S6** and **Figure S7**), the highest LUE of 3.07% was achieved with an AVT of 29.27% at the 75-nm device. The relative TOPVs reaches a PCE of 10.50% with a J_{SC} of 16.42 mA cm^{-2}, a V_{OC} of 0.846 V, and a FF of 75.56% (**Table S**7). For TOPVs with a D:A ratio of 0.5:1.2 (**Figure S8** and **Figure S9**,), the highest LUE of 2.97% was achieved with an AVT of 25.67% at the 120-nm device. The device reaches the PCE of 11.58% with a J_{SC} of 18.18 mA cm^{-2}, a V_{OC} of 0.845 V, and a FF of 75.41% (**Table S**8). The LUE is susceptible to the thickness and ratio of PM6: BTP-eC9 active layer. A decreased PM6 ratio in the active layer is conducive to the LUE improvement for TOPVs. In the binary system, high-performing TOPVs with a LUE of over 3% can thus be obtained with a D: A ratio of 0.8: 1.2.

Ternary strategy is widely utilized to improve the photovoltaic performance of OPVs.[48,49] By adding L8-BO as a third component at the D: A: A ratio of 1: 1: 0.2, the opaque OPVs device achieves a remarkable PCE of 18.24%, with a J_{SC} of 27.10 mA cm^{-2}, a V_{OC} of 0.865 V and a FF of 77.80%. The *J-V* curves and EQE curves of the opaque OPVs with different active layer systems were shown in **Figure S3**. Comparing the performance of binary and ternary devices, the addition of L8-BO leads to an improved PCE resulting from higher V_{OC} and J_{SC} (**Table S**5). The integrated photocurrent from the EQE spectra matches well the J_{SC}s measured from the *J–V* curves. The ternary device exhibits higher EQE at 450-850 nm in comparison to PM6: BTP-eC9 device, which should assist the enhanced J_{SC}. Charge recombination kinetics of the binary and ternary devices were studied. The J_{SC} and V_{OC} versus

light intensity (P_{light}) are plotted in **Figure S10b**. The relationship between the J_{SC} and P_{light} can be expressed by $J_{SC} \propto (P_{light})^{\alpha}$, where α is an exponential factor that reflects the extent of biomolecular charge recombination.[50] The extracted α values for PM6: BTP-eC9 and the PM6: BTP-eC9: L8-BO ternary devices are 0.996 and 0.998, respectively, indicative of weak biomolecular recombination in device. The relationship between V_{OC} and light intensity was studied to further understand the charge recombination behavior (**Figure S10c**). Generally, when the dominant mechanism is bimolecular recombination, a slope of kT/ q (k is the Boltzmann constant, T is the Kelvin temperature, and q is the elementary charge) in the plot of V_{OC} versus the natural logarithm of the light intensity is expected. For trap-assisted recombination, a higher dependence of the V_{OC} on the light intensity (> kT/ q) will be observed.[51] And the slope for PM6: BTP-eC9 and PM6: BTP-eC9: L8-BO blends is 1.055 and 1.043 kT/ q, respectively, suggesting that a small amount of L8-BO in ternary blends can effectively deactivate traps in the host matrix and thereby reduce trap-assisted recombination.

The hole and electron mobilities of the blends were measured by the space charge limited current (SCLC) method (**Table S**9 and **Figure S**11) with configurations of Glass/ ITO/ PEDOT: PSS/ active layer/ MoO_3/ Ag and Glass/ ITO/ ZnO/ active layer/ PDINN/ Ag. The calculated hole/electron (μ_h/ μ_e) mobilities of PM6: BTP-eC9 was 7.60×10^{-4}/ 5.83×10^{-4} cm^2 V^{-1} s^{-1}. While the ternary PM6: BTP-eC9: L8-BO device shows higher hole and electron mobilities of 7.80×10^{-4} and 6.85×10^{-4} cm^2 V^{-1} s^{-1}. Balanced hole/electron transport and high mobilities in PM6: BTP-eC9: L8-BO blends are beneficial to the improved J_{SC} and PCE. The relevant statistical data are plotted in **Figure S**3.

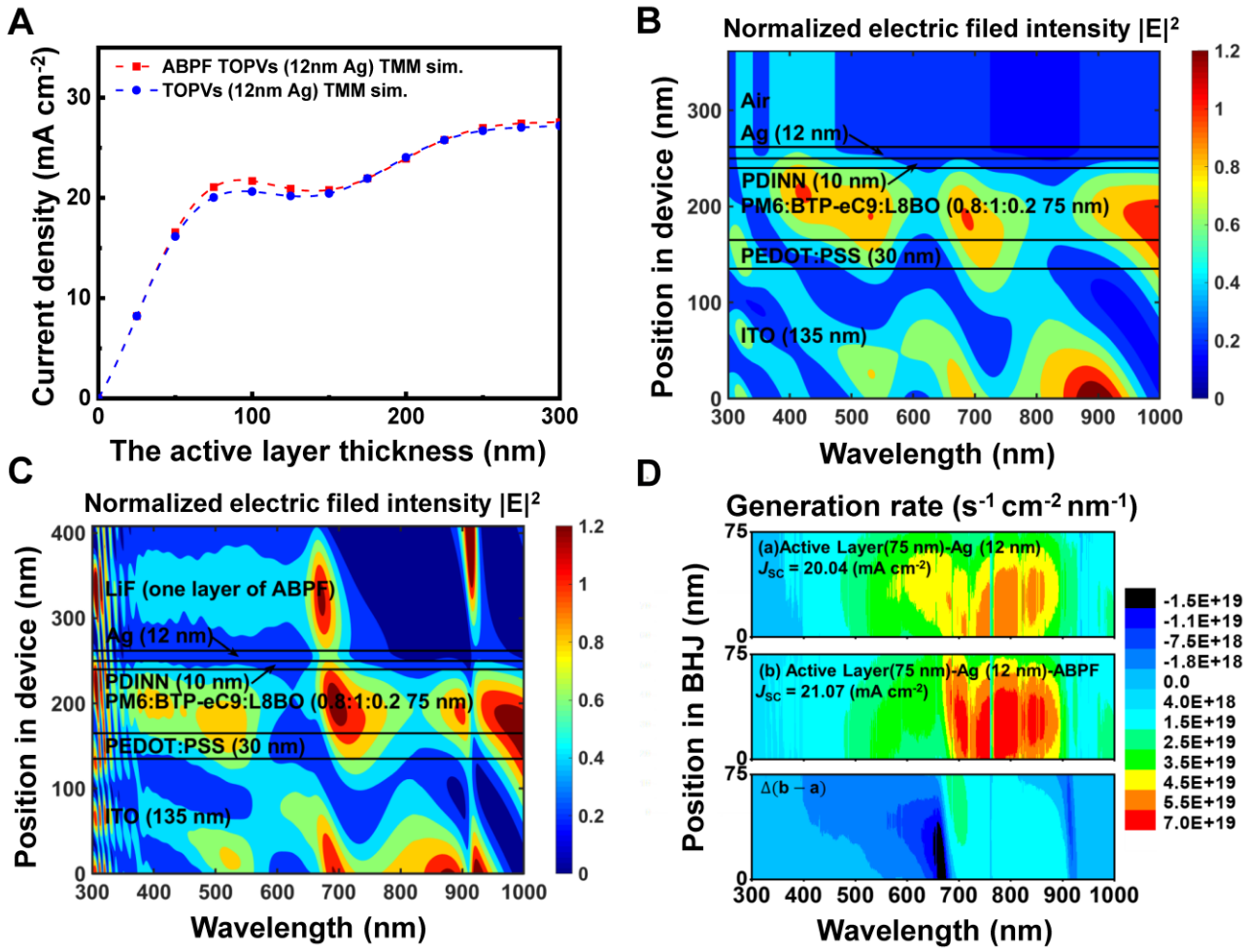

Figure 3. Optical properties of ABPF integrated TOPVs with PM6: BTP-eC9: L8-BO (0.8: 1: 0.2) blends

(A) Simulated J_{SC} of TOPVs with and without ABPF.

(B) Simulated optical filed $|E|^2$ distribution of TOPVs with bare Ag.

(C) Simulated optical filed $|E|^2$ distribution of ABPF integrated TOPVs

(D) Simulation of the exciton generation in devices with and without ABPF.

For TOPVs, the ratio of PM6: BTP-eC9: L8-BO is also optimized (**Figure S**12-15, **Table S**10-11). At similar thickness, compared to the binary device (0.8: 1.2 of 75-nm PM6: BTP-eC9) counterpart, the ternary (0.8:1.0:0.2) TOPVs exhibited a higher *J*sc and *V*oc, resulting in an enhancement of 6% in PCE. Further, the AVT is increased from 29.27% to 29.71%, so an enhancement of 8% in LUE can be

achieved in ternary TOPVs. For the same composition of BHJ blends (Table S10), the BHJ thickness is closely related to the device transmittance and photon harvesting, resulting in varying AVT and J_{SC}. When the active layer thickness is over 75 nm, a slowly increasing J_{SC} and a linearly descending AVT occur along with the increased active layer thickness, resulting in slightly lower LUE. By integrating the ternary strategy (PM6: BTP-eC9: L8-BO) and tuning ratio (0.8:1:0.2), thickness (75 nm) of active layer, a considerable LUE of 3.31% for TOPVs was achieved with a PCE of 11.15% and an AVT of 29.71% (**Table 1**).

The simulations of the photocurrent density and optoelectronic field intensity distribution in the TOPVs with and without ABPF are carried out to reveal the effect of the optical capping layer on the optical interference. By assuming the internal quantum efficiency (IQE) is equal to 100% of all wavelengths, the simulated J_{SC} curve shows common oscillating characteristics due to coherent interference. The simulated J_{SC} of the devices first increases when the thickness of blends is increased from 0 to 75 nm, and then flattens from 75 to 150 nm. And the J_{SC} of ABPF integrated TOPVs is slightly higher than the counterpart one as shown in **Figure 3A**. The optical filed $|E|^2$ distribution and exciton generation rates of relative TOPVs (75-nm active layer) are carried out (**Figure 3**B and **Figure 3**C). ABPF integrated TOPV exhibits lower simulated electric field intensity than the counterpart without ABPF in the visible region. In the NIR region, TOPV with ABPF exhibits an apparent increased electric field intensity. To reveal the effect of ABPF on the photovoltaic performance visually, the exciton generation rates of 75-nm TOPVs with and without ABPF are simulated as shown in **Figure**

3D. The simulated J_{SC} is 21.07, and 20.04 mA cm^{-2} for TOPVs with and without ABPF, respectively. The difference in the exciton generation rate of TOPVs with and without ABPF is calculated by subtracting the value of Ag-based device with ABPF integrated device. The difference in exciton generation rate is negative between 300 and 700 nm (10^{18}~10^{19} s^{-1} cm^{-2} nm^{-1}), resulting in a decreased simulated J_{SC} (1.19 mA cm^{-2}). While there appears to be a positive variation between 700 and 1000 nm (10^{19} s^{-1} cm^{-2} nm^{-1}), contributing an increased simulated J_{SC} (2.22 mA cm^{-2}). The equalizing influence in the whole region (300-1000 nm) is consistent with the trend of simulated J_{SC} difference for TOPVs with and without ABPF, indicating the effective optical management of ABPF in device with a higher absorbing selectivity (**Table S**12).

The above-discussed results reveal the potential of ABPF for high-performance TOPVs. The optimal condition of PM6: BTP-eC9: L8-BO (0.8: 1: 0.2) was explored for TOPVs integrating ABPF and ARC. The detailed *J–V* curves, EQE curves, and optical transmittance spectra and the colored coordinates for ABPF and ARC integrated TOPVs are shown in **Figure S16**. Along with the decreased thickness of active layer, the transmittance of the ABPF-integrated TOPVs in the visible region increases significantly, while the almost zero transmission in the range of 700-900 nm remains unchanged. The corresponding photovoltaic performance and optical properties of TOPVs with ABPF are summarized in **Table S13**. At the thickness (active layer) of 75 nm, the ABPF integrated TOPVs exhibited a PCE of 11.44%, an AVT of 46.79%, and the highest LUE of 5.35% (**Figure 4**A). Remarkable LUEs of over 5% in devices are attained when active layer thickness is adjusted from 65 nm to 90 nm. At the

thickness (active layer) of 65 nm, the ABPF integrated TOPVs exhibited a high AVT over 50% with a LUE of 5.16%. A high PCE of 15.10% was obtained with an AVT of 25.08% in 140-nm BHJ based devices. In relative to the counterparts without ABPF, the TOPVs with ABPF demonstrated remarkable ~60% enhancement in AVT and LUE, with slight enhancement in PCE. Similar enhancements are shown in binary TOPVs too (**Figure S17 and Table S14**). Compared with TOPVs based on bare 12-nm Ag, ABPF integrated TOPVs exhibited higher AVT value and thus lower EQE in the range of 400-700 nm, and much enhanced EQE response and an optical band-stop in the NIR region. As shown in **Figure S18**, the change of EQE from 400 to 900 nm corresponds to the variation of the exciton generation rate between TOPVs with and without ABPF, which is consistent with the above-simulated results. The individual role of ARC and ABPF on the device performance was investigated by fabricating ARC/TOPVs and TOPVs/ABPF devices based on 75-nm PM6:BTP-eC9:L8-BO (0.8:1.0:0.2) ternary systems (**Figure S**19 and **Table S**15). In relative to the counterparts without ARC, the ARC/TOPVs demonstrated ~3% enhancement in AVT and LUE, with slight enhancement in J_{SC} and PCE. The ABPF integrated TOPVs exhibited remarkable ~55% enhancement in AVT and LUE. As a result, the champion device of ARC-ABPF-integrated TOPVs achieved the highest LUE values as high as 5.35%. The bifacial performance of the champion device was also investigated. As shown in **Figure S**20 and **Table S**16, TOPVs exhibited poor performance due to the low J_{SC} of 6.19 mA cm^{-2} when the light is illuminated from the ABPF side. The relative EQE response of TOPVs is almost zero at 700-900 nm, resulting in a low J_{SC}. The EQE + transmission (T) + reflection (R) of ABPF

integrated TOPVs devices are also measured to further validate the full optical analysis. The value is below 1, indicating the accuracy and reliability of the data in this study (**Figure S**21). The ABPF is also stable as expected from inorganic compounds. The transmittance of the ABPF integrated device is unchanged under thermal annealing and prolonged continuous illumination as shown in **Figure S**22. The stability data under the maximum power point (MPP) tracking were summarized as shown in Figure S22c. Although 100-nm Ag based OPV without encapsulation exhibited a slightly improved stability than bare 12-nm Ag based TOPV without encapsulation, both the devices degrade sharply in 2 h. The PCEs of ABPF based TOPV without encapsulation retain 70% of their original values after a 50 h MPP tracking test. To reveal the impact of ABPF structure against moisture and oxygen intuitively, equivalent encapsulation tests have been conducted as indicated in Figure S23. Calcium metal is very sensitive to oxygen and moisture, and is widely used in OLED industry to test encapsulation and stability. We fabricated controlled devices without or with ABPF electrodes using calcium metal as the testing layer. The devices were kept in the air, and the variations of their transmittances were measured as shown in **Figure S**23. After a long period (80 hours) of storage in the air, the transmittance of the devices without ABPF increased dramatically, demonstrating oxidation of Ca, and thus poor oxygen and moisture barrier properties of bare thin Ag-covered films. While the transmittance curve of the ABPF-integrated device changed much slower, indicating the barrier property of ABPF-integrated devices was significantly improved. The results of equivalent encapsulation tests indicate that the ABPF structure can prolong the active layer's exposure to moisture and oxygen to some extent,

resulting in improved device stability. Furthermore, both the encapsulated ABPF based TOPV and 12-nm Ag based TOPV exhibit considerable operational stability, remaining 82% and 77% of their original values after a 350-h MPP tracking test, respectively.

Meanwhile, by calculating limiting efficiencies for single-junction OPVs as a function of bandgap for transparent architectures with varied EQE contributions from the visible part of the spectrum in **Figure S**24. The corresponding relationship between the visible EQE contribution and AVT can be approximated by EQE + AVT = 1 in the absence of reflection losses. Assuming E_{loss} of 0.5 eV and FF of 80%, a theoretical LUE value of 8.5% with an AVT of 50% can be obtained through integrating an ideal band-pass filter (ABPF), indicating the potential for future TOPVs and further materials development.

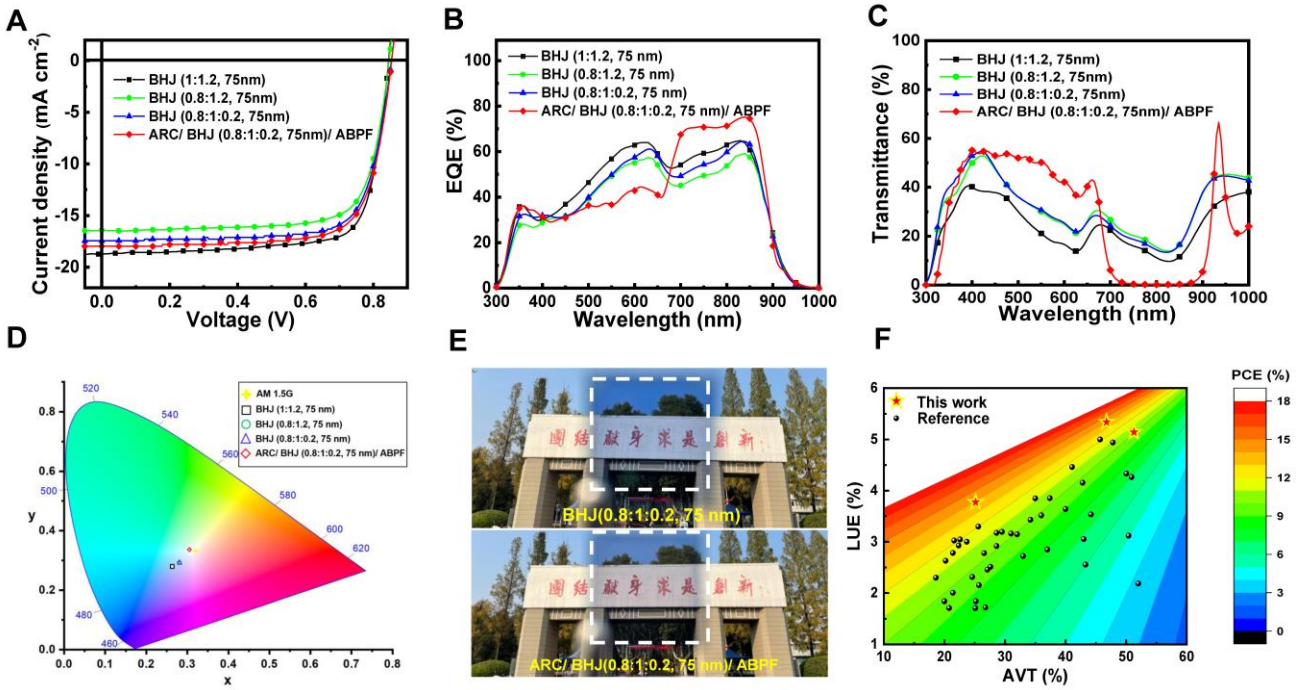

Figure 4. Photovoltaic performance and optical properties of TOPVs with and without ABPF.

(A) *J–V* curves.

(B) EQE curves.

(C) Transmittance spectra curves.

(D) Color coordinates of TOPVs based on the CIE 1931 chromaticity diagram.

(E) Photographs of TOPVs with and without ABPF using Nanjing University of Science and Technology landmark as background.

(F) Summary of the reported PCE and AVT of TOPVs.

Table 1 The photovoltaic and optical performance of the binary and ternary systems the bare 12-nm Ag and ABPF based TOPVs with 75-nm active layer thickness.

Active layer	J_{SC} (mA cm^{-2})	J_{SC}[a] (mA cm^{-2})	V_{OC} (V)	FF (%)	PCE (%)	AVT (%)	LUE (%)	CIE1931	CRI
PM6: BTP-eC9 (1:1.2)[b]	18.73 (18.38±0.33)	18.19	0.845 (0.843±0.02)	75.21 (74.84±0.36)	11.90 (11.60±0.29)	21.03	2.50	(0.264,0.281)	73.61
PM6: BTP-eC9 (0.8:1.2)[b]	16.42 (16.12±0.28)	15.94	0.846 (0.843±0.03)	75.56 (75.12±0.42)	10.5 (10.21±0.27)	29.27	3.07	(0.280,0.293)	80.29
PM6: BTP-eC9 (0.5:1.2)[b]	12.39 (12.01±0.35)	12.05	0.840 (0.837±0.03)	74.83 (74.33±0.46)	7.79 (7.47±0.30)	36.22	2.82	(0.296,0.315)	84.41
PM6: BTP-eC9: L8-BO (0.8: 1.0: 0.2)[b]	17.44 (17.14±0.28)	16.95	0.853 (0.851±0.02)	74.93 (74.40±0.45)	11.15 (10.85±0.27)	29.71	3.31	(0.281,0.293)	80.27
PM6: BTP-eC9: L8-BO (0.5: 1.0: 0.2)[b]	12.82 (12.51±0.30)	12.74	0.847 (0.846±0.01)	74.77 (74.31±0.45)	8.12 (7.86±0.29)	35.19	2.86	(0.293,0.308)	83.98
PM6: BTP-eC9: L8-BO (0.8: 1.0: 0.2)[c]	17.97 (17.57±0.35)	17.45	0.854 (0.852±0.01)	74.54 (74.12±0.39)	11.44 (11.10±0.31)	46.79	5.35	(0.305,0.336)	85.39

[a]The J_{SC} values are integrated from EQE curves. Average values with standard deviation are obtained from 12 devices.

[b]The bare 12-nm Ag based TOPVs

[c]The ABPF based TOPVs

The CRI and the color-coordinated (x, y) are other important criteria to evaluate the performance of TOPVs. The AM 1.5G exhibits a CIE 1931 coordinates of AM 1.5G (0.3202, 0.3324) and a CCT of 5513 K. For the binary TOPVs (75 nm), the CRI increases from 73.61 to 84.41 and the CIE color coordinates shifts from (0.264,0.281) to (0.296,0.315) when the D: A ratio is varied from 1: 1.2 to 0.5: 1.2. A decreased PM6 ratio in blends is beneficial for an improved CRI value of TOPVs (**Figure 4**D). For the PM6: BTP-eC9: L8-BO (0.8: 1: 0.2) based TOPVs with ABPF, CRI increases to 85.39 with the CIE color coordinates (0.305,0.336) as summarized in **Table 1**. As shown in **Figure 4**E, scaled-up ternary TOPVs with and without ABPF are fabricated to explore the influence on the color-rendering capacity. The visibility and vivid color of the Nanjing University of Science and Technology landmark as background can be seen more clearly after integrating ABPF into TOPVs, indicating the great potential in building integrated photovoltaic applications, etc. It is worth noting that TOPV with ABPF achieves the highest LUE values as high as 5.35% with a PCE of 11.44%, an AVT of 46.79%, and a CRI of 85.39 (**Figure. 4**F **and Table S**17).

Conclusions

To summarize, we successfully design and construct high-performance TOPVs with the architecture of $(LiF/ TeO_2)^4$/ Glass/ ITO/ PEDOT: PSS/ PM6: BTP-eC9: L8-BO (0.8:1:0.2)/ PDINN/ Ag (12nm)/ $(LiF/ TeO_2)^8$ /LiF. A versatile aperiodic band-pass filter (ABPF, aperiodic $(LiF/ TeO_2)^8$ /LiF) with an AVT of up to 78.69% and CRI of 97.54 in the visible region and almost total reflection in the NIR region (700-900 nm) has been achieved. The performance of TOPVs is systematically influenced by

the composition ratio and thickness of PM6: BTP-eC9: L8-BO BHJ films. By integrating the ternary strategy (PM6: BTP-eC9: L8-BO) and tuning ratio (0.8: 1: 0.2), thickness (75 nm) of active layer, the relative ABPF integrated TOPVs demonstrate the record LUE of 5.35%, accompanied with PCE of 11.44%, AVT of 46.79%, CIE coordinates of (0.305, 0.336), and CRI of 85.39. Remarkable LUEs of over 5% in devices are attained when active layer thickness is adjusted from 65 nm to 90 nm. At the thickness (active layer) of 65 nm, the ABPF integrated TOPVs exhibited a high AVT over 50% with a LUE of 5.16%, a record for any TOPVs with 50% AVT. Also a record high PCE of 15.10% was obtained with an AVT of over 25% in 140-nm BHJ based devices. In relative to the counterparts without ABPF, the TOPVs with ABPF demonstrated remarkable ~60% enhancement in AVT and LUE, with slight enhancement in PCE. To our best knowledge, the LUE of 5.35% as the figure of merit for single-junction TOPVs is the highest value in the literature. Furthermore, the ABPF structure can prolong the active layer's exposure to moisture and oxygen to some extent, resulting in improved device stability. This optical design of aperiodic band-pass electrode can be universally applied to high-efficiency TOPVs, thereby significantly promoting the commercialization potential of TOPVs.

EXPERIMENTAL PROCEDURES

Optical Simulation

Optical modeling with the transfer matrix method was employed to calculate the transmittance, optical electric field intensity, and exciton generation rate distribution in devices.[52] All the simulations of optical properties and exciton generation are based on the assumptions of planar interfaces and isotropy

for the layers within the devices.[53] The optical properties of each layer are represented by the indexes of refraction (η+ iκ), measured using a variable angle spectroscopic ellipsometer (WVASE32, J. A. Woollam, VB400). To calculate the exciton generation rate, theoretical maximum photocurrent density and loss portion in the simulated J_{SC}, 100% IQE, and the AM1.5 intensity spectrum (ASTM G173–03) are assumed. The generation of excitons in the active layer is described by considering the following parameters: the modulus squared of the electric field obtained from TMM, the AM1.5G spectrum, the real part of the refractive index (η), and the absorption coefficient (α), which is associated to the imaginary part (κ) of the refractive index by $\alpha = 4\pi\kappa/\lambda$ and the factor $c\varepsilon_0/2$, where c is the speed of light in vacuum and ε_0 the permittivity of free space.

Materials and Solution Preparations

PEDOT: PSS (CLEVIOS™ P VP AI 4083) was purchased from Heraeus. PM6, BTP-eC9 and L8-BO were purchased from Solarmer Materials Inc. PDINN was purchased from Suna Tech Inc. The solvents and other materials were purchased from Sigma-Aldrich. All reagents were used directly.

Device Fabrications

ITO-coated glass substrates (15 Ω sq^{-1}) were cleaned via sequential ionization in detergent, deionized water, acetone, and isopropanol. All pre-cleaned ITO substrates were treated by oxygen plasma for 180 seconds to increase work function and clearance. PEDOT: PSS layer (30 nm) was spin-coated at a speed of 3500 rpm onto the ITO glass, and annealed at 150 for 15 min. For the binary system, PM6: BTP-eC9 was dissolved in Chlorobenzene with a total concentration of 22 mg ml^{-1} (D: A = 1:1.2), 20

mg ml^{-1} (D: A = 0.8: 1.2), 17 mg ml^{-1} (D: A = 0.5: 1.2). For the ternary system, PM6: BTP-eC9: L8-BO were dissolved in chlorobenzene with a total concentration of 20 $mgml^{-1}$ (D: A: A= 0.8: 1: 0.2) and 17 mg ml^{-1} (D: A: A= 0.5: 1: 0.2). The solutions were stirred at room temperature. Before spin-coating the active layer, 1,8-diiodooctane (DIO, 0.5% v/ v) was added. The active layer film was spin-coated on the PEDOT: PSS layer in a nitrogen-filled glove box and thermal annealing treatment at 100 °C for 10 min. Then methanol solution of PDINN at a concentration of 1.0 mg ml^{-1} was deposited on the active layer at 3000 rpm for 30s to afford a cathode buffer layer.

The ultrathin Ag rear electrode is evaporated via a thermal evaporator through a shadow mask with a rate of 3.0 Å s^{-1} under $2.0*10^{-4}$ Torr, which defines the active cell area of 0.04 cm^2 through an optical microscope. The band-pass filter was grown by vacuum thermal evaporation in a chamber with a base pressure of 2.0×10^{-6} Torr at 2.0 Å s^{-1} for LiF and 1.0 Å s^{-1} for TeO_2.

Device Characterizations

Device performance was measured in a glove box. To improve the accuracy of measurement, the *J-V* curves of all devices were measured by masking the active area with a metal mask of 0.0324 cm^2, which defines the illumination area to be 0.0324 cm^2. The *J–V* curves of devices were determined under AM 1.5G illumination (100 mW cm^{-2}) using a computer-controlled Keithley 2400 source measurement unit and a calibrated solar simulator (Enli Technology Co. Ltd), and no applied bias or light soaking process was applied before *J-V* measurement. A standard Si secondary reference cell cover with a KG-5 filter was utilized to calibrate the illumination intensity, giving a value of 100 mW

cm^{-2} in the test. All the *J-V* curves reported in this manuscript were tested by sweeping the *J-V* measurement from the forward direction (from short-circuit to open-circuit) with a step of 0.02 V. The delay time is set to zero. EQE and reflection spectra were measured by using a Solar Cell Spectral Response Measurement System QE-R3011 (Enlitech). The thickness was measured from a Bruker DektakXT Surface Profiler. The absorption and transmission spectra were measured using a UV-vis spectrometer (Persee, TU-1810), and air was used as the reference to make the transmittance as an absolute value. The device stability of optical performance under thermal annealing and prolonged continuous illumination was tested in a N_2-filled glovebox. The device stability of photovoltaic performance was measured with MPP tracking test under one sun illumination (LED lamp, Enlitech product) in the ambient air condition. The illumination intensity was controlled to provide an output of 100 mW cm^{-2} during the aging period. The encapsulated device was using an ultraviolet-curable epoxy by bonding a glass. The stage temperature was kept at ~ 25 ℃. The PCEs of OPVs without encapsulation were recorded every 15 min to collect more data due to the rapid degradation. The PCEs of TOPVs with encapsulation were recorded every 1 h.

Optical Properties

It should be emphasized that the measured AVT value is different from the human eye perception. The AVT value is determined by calculating the average value of transmittance of the transparent device in the visible light wavelength range (380 nm–740 nm) based on the photonic response of the human eye. The AVT value of TOPVs can be calculated according to the following equation:

$$\mathrm{AVT} = \frac{\int T(\lambda) \times P(\lambda) \times AM1.5G(\lambda)\, d(\lambda)}{\int P(\lambda) \times AM1.5G(\lambda)\, d(\lambda)}$$

Where T(λ) is the transmission spectrum of TOPVs, P(λ) is the photopic response of the human eye, AM1.5G(λ) is photon flux under AM 1.5G light illumination conditions.[39]

The CIE 1931 xyz chromaticity diagram, as designed for human eye perception, can be used to evaluate the color property of illuminants. The color coordinate (x, y, z) of TOPVs can be calculated according to the corresponding transmitted light. The sum of color coordinates (x, y, z) is equal to 1, and the color coordinates can be simplified to two-dimensional coordinates (x, y). Standard daylight illuminant AM 1.5G (0.3202, 0.3324) and D65 (0.3128, 0.3290) are commonly chosen as reference light sources for evaluating the color property of transparent OPVs.[54] The color coordinates of neutral color TOPVs are close to (0.3333, 0.3333) or that of illuminant AM 1.5G and D65, which are generally preferred for solar widow application.

The CRI is another important parameter to evaluate the performance of TOPVs. The value of CRI can be obtained by comparing the color rendering of a reference light source to that of a test light source, which can quantitatively exhibit the ability of a test light source to reveal the color of an object compared with a reference or natural light source. The CRI value is defined as the value from 0 to 100, a higher CRI represents better color rendering ability and higher neutral color degree. For the TOPVs, the CRI can be evaluated according to the matching degree between the transmitted light from the devices and the illumination light.

SUPPLEMENTAL INFORMATION

Supplemental Information includes ten figures and two tables and can be found on-line at https://doi.org/.

ACKNOWLEDGMENTS

The authors gratefully acknowledge the financial support from the National Natural Science Foundation of China (Grant No. 21905137). J. Yu thanks the support from the Hong Kong Scholar Program (XJ2020042). G. Li thanks support from Research Grants Council of Hong Kong (Project nos.15221320, C5037-18G), Guangdong-Hong Kong-Macao Joint Laboratory for Photonic-Thermal-Electrical Energy Materials and Devices (GDSTC no. 2019B121205001), Hong Kong Polytechnic University (the Sir Sze-yuen Chung Endowed Professorship Fund (8-8480), CDA5, YWAH and SAC5).

AUTHOR CONTRIBUTIONS

Jiangsheng Yu and Xin Liu conceived the idea. Xin Liu carried out the device fabrication, simulation, and characterization. Ziping Zong helped in the experiment. All authors participated in the analysis and discussions of the results. Xin Liu wrote the original draft. Jiangsheng Yu and Gang Li reviewed and edited the writing, planned and directed the project.

DECLARATION OF INTERESTS

The authors declare no competing interests.

References

1. Bae, S.-H., Zhao, H., Hsieh, Y.-T., Zuo, L., De Marco, N., Rim, You S., Li, G., and Yang, Y. (2016). Printable Solar Cells from Advanced Solution-Processible Materials. Chem *1*, 197-219.

2. Cheng, P., Li, G., Zhan, X., and Yang, Y. (2018). Next-generation organic photovoltaics based on non-fullerene acceptors. Nat. Photonics *12*, 131-142.

3. Hou, J., Inganäs, O., Friend, R.H., and Gao, F. (2018). Organic solar cells based on non-fullerene acceptors. Nat. Mater. *17*, 119-128.

4. Li, Y., Xu, G., Cui, C., and Li, Y. (2018). Flexible and Semitransparent Organic Solar Cells. Adv. Energy Mater. *8*, 1701791.

5. Shi, H., Xia, R., Zhang, G., Yip, H.-L., and Cao, Y. (2019). Spectral Engineering of Semitransparent Polymer Solar Cells for Greenhouse Applications. Adv. Energy Mater. *9*, 1803438.

6. Wang, J., Zheng, Z., Zu, Y., Wang, Y., Liu, X., Zhang, S., Zhang, M., and Hou, J. (2021). A Tandem Organic Photovoltaic Cell with 19.6% Efficiency Enabled by Light Distribution Control. Adv. Mater. *33*, 2102787.

7. Zheng, Z., Wang, J., Bi, P., Ren, J., Wang, Y., Yang, Y., Liu, X., Zhang, S., and Hou, J. (2022). Tandem Organic Solar Cell with 20.2% Efficiency. Joule *6*, 171-184.

8. Forberich, K., Guo, F., Bronnbauer, C., and Brabec, C.J. (2015). Efficiency Limits and Color of Semitransparent Organic Solar Cells for Application in Building-Integrated Photovoltaics. Energy Technol. *3*, 1051-1058.

9. Ballif, C., Perret-Aebi, L.-E., Lufkin, S., and Rey, E. (2018). Integrated thinking for photovoltaics in buildings. Nat. Energy *3*, 438-442.

10. Chang, S.-Y., Cheng, P., Li, G., and Yang, Y. (2018). Transparent Polymer Photovoltaics for Solar Energy Harvesting and Beyond. Joule *2*, 1039-1054.

11. Sun, C., Xia, R., Shi, H., Yao, H., Liu, X., Hou, J., Huang, F., Yip, H.-L., and Cao, Y. (2018). Heat-Insulating Multifunctional Semitransparent Polymer Solar Cells. Joule *2*, 1816-1826.

12. Xue, Q., Xia, R., Brabec, C.J., and Yip, H.-L. (2018). Recent advances in semi-transparent polymer and perovskite solar cells for power generating window applications. Energy Environ. Sci. *11*, 1688-1709.

13. Liu, Y., Cheng, P., Li, T., Wang, R., Li, Y., Chang, S.Y., Zhu, Y., Cheng, H.W., Wei, K.H., Zhan, X., et al. (2019). Unraveling Sunlight by Transparent Organic Semiconductors toward Photovoltaic and Photosynthesis. ACS Nano *13*, 1071-1077.

14. Li, Y., Guo, X., Peng, Z., Qu, B., Yan, H., Ade, H., Zhang, M., and Forrest, S.R. (2020). Color-neutral, semitransparent organic photovoltaics for power window applications. Proc. Natl. Acad. Sci.

U.S.A. *117*, 21147-21154.

15. Pascual-San-José, E., Sadoughi, G., Lucera, L., Stella, M., Martínez-Ferrero, E., Morse, G.E., Campoy-Quiles, M., and Burgués-Ceballos, I. (2020). Towards photovoltaic windows: scalable fabrication of semitransparent modules based on non-fullerene acceptors via laser-patterning. J. Mater. Chem. A *8*, 9882-9895.

16. Ravishankar, E., Booth, R.E., Saravitz, C., Sederoff, H., Ade, H.W., and O'Connor, B.T. (2020). Achieving Net Zero Energy Greenhouses by Integrating Semitransparent Organic Solar Cells. Joule *4*, 490-506.

17. Song, W., Fanady, B., Peng, R., Hong, L., Wu, L., Zhang, W., Yan, T., Wu, T., Chen, S., and Ge, Z. (2020). Foldable Semitransparent Organic Solar Cells for Photovoltaic and Photosynthesis. Adv. Energy Mater. *10*, 2000136.

18. Zhang, N., Jiang, T., Guo, C., Qiao, L., Ji, Q., Yin, L., Yu, L., Murto, P., and Xu, X. (2020). High-performance semitransparent polymer solar cells floating on water: Rational analysis of power generation, water evaporation and algal growth. Nano Energy *77*, 105111.

19. Wang, D., Liu, H.R., Li, Y.H., Zhou, G.Q., Zhan, L.L., Zhu, H.M., Lu, X.H., Chen, H.Z., and Li, C.Z. (2021). High-performance and eco-friendly semitransparent organic solar cells for greenhouse applications. Joule *5*, 945-957.

20. Ravishankar, E., Booth, R.E., Hollingsworth, J.A., Ade, H., Sederoff, H., DeCarolis, J.F., and O'Connor, B.T. (2022). Organic solar powered greenhouse performance optimization and global economic opportunity. Energy Environ. Sci. *15*, 1659-1671.

21. Traverse, C.J., Pandey, R., Barr, M.C., and Lunt, R.R. (2017). Emergence of highly transparent photovoltaics for distributed applications. Nat. Energy *2*, 849-860.

22. Czolk, J., Puetz, A., Kutsarov, D., Reinhard, M., Lemmer, U., and Colsmann, A. (2013). Inverted Semi-transparent Polymer Solar Cells with Transparency Color Rendering Indices approaching 100. Adv. Energy Mater. *3*, 386-390.

23. Zhang, J., Xu, G., Tao, F., Zeng, G., Zhang, M., Yang, Y.M., Li, Y., and Li, Y. (2019). Highly Efficient Semitransparent Organic Solar Cells with Color Rendering Index Approaching 100. Adv. Mater. *31*, 1807159.

24. Hu, Z., Wang, Z., An, Q., and Zhang, F. (2020). Semitransparent polymer solar cells with 12.37% efficiency and 18.6% average visible transmittance. Sci. Bull. *65*, 131-137.

25. Yin, P., Yin, Z., Ma, Y., and Zheng, Q. (2020). Improving the charge transport of the ternary blend active layer for efficient semitransparent organic solar cells. Energy Environ. Sci. *13*, 5177-5185.

26. Lu, X., Cao, L., Du, X., Lin, H., Zheng, C., Chen, Z., Sun, B., and Tao, S. (2021). Hydrogen-Bond-Induced High Performance Semitransparent Ternary Organic Solar Cells with 14% Efficiency

and Enhanced Stability. Adv. Opt. Mater. *9*, 2100064.

27. Zhu, R., Chung, C.-H., Cha, K.C., Yang, W., Zheng, Y.B., Zhou, H., Song, T.-B., Chen, C.-C., Weiss, P.S., Li, G., and Yang, Y. (2011). Fused Silver Nanowires with Metal Oxide Nanoparticles and Organic Polymers for Highly Transparent Conductors. ACS Nano *5*, 9877-9882.

28. Beiley, Z.M., Christoforo, M.G., Gratia, P., Bowring, A.R., Eberspacher, P., Margulis, G.Y., Cabanetos, C., Beaujuge, P.M., Salleo, A., and McGehee, M.D. (2013). Semi-Transparent Polymer Solar Cells with Excellent Sub-Bandgap Transmission for Third Generation Photovoltaics. Adv. Mater. *25*, 7020-7026.

29. Chen, C.-C., Dou, L., Gao, J., Chang, W.-H., Li, G., and Yang, Y. (2013). High-performance semi-transparent polymer solar cells possessing tandem structures. Energy Environ. Sci. *6*, 2714-2720.

30. Min, J., Bronnbauer, C., Zhang, Z.-G., Cui, C., Luponosov, Y.N., Ata, I., Schweizer, P., Przybilla, T., Guo, F., Ameri, T., et al. (2016). Fully Solution-Processed Small Molecule Semitransparent Solar Cells: Optimization of Transparent Cathode Architecture and Four Absorbing Layers. Adv. Funct. Mater. *26*, 4543-4550.

31. Ji, G., Wang, Y., Luo, Q., Han, K., Xie, M., Zhang, L., Wu, N., Lin, J., Xiao, S., Li, Y.-Q., et al. (2018). Fully Coated Semitransparent Organic Solar Cells with a Doctor-Blade-Coated Composite Anode Buffer Layer of Phosphomolybdic Acid and PEDOT:PSS and a Spray-Coated Silver Nanowire Top Electrode. ACS Appl. Mater. Interfaces *10*, 943-954.

32. Jeong, H.I., Biswas, S., Yoon, S.C., Ko, S.J., Kim, H., and Choi, H. (2021). Rational Design of Highly Efficient Semi-Transparent Organic Photovoltaics with Silver Nanowire Top Electrode via 3D Optical Simulation Study. Adv. Energy Mater. *11*, 2102397.

33. Dong, Q., Zhou, Y., Pei, J., Liu, Z., Li, Y., Yao, S., Zhang, J., and Tian, W. (2010). All-spin-coating vacuum-free processed semi-transparent inverted polymer solar cells with PEDOT:PSS anode and PAH-D interfacial layer. Org. Electron. *11*, 1327-1331.

34. Fan, X., Xu, B., Liu, S., Cui, C., Wang, J., and Yan, F. (2016). Transfer-Printed PEDOT:PSS Electrodes Using Mild Acids for High Conductivity and Improved Stability with Application to Flexible Organic Solar Cells. ACS Appl. Mater. Interfaces *8*, 14029-14036.

35. Bauer, A., Wahl, T., Hanisch, J., and Ahlswede, E. (2012). ZnO:Al cathode for highly efficient, semitransparent 4% organic solar cells utilizing TiOx and aluminum interlayers. Appl. Phys. Lett. *100*, 073307.

36. Liu, Z., You, P., Liu, S., and Yan, F. (2015). Neutral-Color Semitransparent Organic Solar Cells with All-Graphene Electrodes. ACS Nano *9*, 12026-12034.

37. Song, Y., Chang, S., Gradecak, S., and Kong, J. (2016). Visibly-Transparent Organic Solar Cells on Flexible Substrates with All-Graphene Electrodes. Adv. Energy Mater. *6*, 1600847.

38. Shin, D.H., Jang, C.W., Lee, H.S., Seo, S.W., and Choi, S.-H. (2018). Semitransparent Flexible Organic Solar Cells Employing Doped-Graphene Layers as Anode and Cathode Electrodes. ACS Appl. Mater. Interfaces *10*, 3596-3601.

39. Lunt, R.R. (2012). Theoretical limits for visibly transparent photovoltaics. Appl. Phys. Lett. *101*, 043902.

40. Zuo, L., Shi, X., Fu, W., and Jen, A.K.-Y. (2019). Highly Efficient Semitransparent Solar Cells with Selective Absorption and Tandem Architecture. Adv. Mater. *31*, 1901683.

41. Li, Y., He, C., Zuo, L., Zhao, F., Zhan, L., Li, X., Xia, R., Yip, H.-L., Li, C.-Z., Liu, X., and Chen, H. (2021). High-Performance Semi-Transparent Organic Photovoltaic Devices via Improving Absorbing Selectivity. Adv. Energy Mater. *11*, 2003408.

42. Betancur, R., Romero-Gomez, P., Martinez-Otero, A., Elias, X., Maymó, M., and Martorell, J. (2013). Transparent polymer solar cells employing a layered light-trapping architecture. Nat. Photonics *7*, 995-1000.

43. Xia, R., Brabec, C.J., Yip, H.-L., and Cao, Y. (2019). High-Throughput Optical Screening for Efficient Semitransparent Organic Solar Cells. Joule *3*, 2241-2254.

44. Zhang, Y., Peng, Z., Cai, C., Liu, Z., Lin, Y., Zheng, W., Yang, J., Hou, L., and Cao, Y. (2016). Colorful semitransparent polymer solar cells employing a bottom periodic one-dimensional photonic crystal and a top conductive PEDOT:PSS layer. J. Mater. Chem. A *4*, 11821-11828.

45. Li, Y., Ji, C., Qu, Y., Huang, X., Hou, S., Li, C.Z., Liao, L.S., Guo, L.J., and Forrest, S.R. (2019). Enhanced Light Utilization in Semitransparent Organic Photovoltaics Using an Optical Outcoupling Architecture. Adv. Mater. *31*, 1903173.

46. Shen, P., Yao, M., Liu, J., Long, Y., Guo, W., and Shen, L. (2019). Colored semitransparent polymer solar cells with a power conversion efficiency of 9.36% achieved by controlling the optical Tamm state. J. Mater. Chem. A *7*, 4102-4109.

47. Liu, X., Zhao, Y., Yu, J., and Zhu, R. (2021). High-performance bifacial semitransparent organic photovoltaics featuring a decently transparent TeO2/Ag electrode. Mater. Chem. Front. *5*, 8197-8205.

48. Zuo, L., Jo, S.B., Li, Y., Meng, Y., Stoddard, R.J., Liu, Y., Lin, F., Shi, X., Liu, F., Hillhouse, H.W., et al. (2022). Dilution effect for highly efficient multiple-component organic solar cells. Nat. Nanotechnol. *17*, 53-60.

49. Li, Y., Guo, Y., Chen, Z., Zhan, L., He, C., Bi, Z., Yao, N., Li, S., Zhou, G., Yi, Y., et al. (2022). Mechanism study on organic ternary photovoltaics with 18.3% certified efficiency: from molecule to device. Energy Environ. Sci. *15*, 855-865.

50. Kyaw, A.K.K., Wang, D.H., Gupta, V., Leong, W.L., Ke, L., Bazan, G.C., and Heeger, A.J. (2013). Intensity Dependence of Current-Voltage Characteristics and Recombination in High-Efficiency

Solution-Processed Small-Molecule Solar Cells. ACS Nano *7*, 4569-4577.

51. Koster, L.J.A., Mihailetchi, V.D., Ramaker, R., and Blom, P.W.M. (2005). Light intensity dependence of open-circuit voltage of polymer:fullerene solar cells. Appl. Phys. Lett. *86*, 123509.

52. Pettersson, L.A.A., Roman, L.S., and Inganäs, O. (1999). Modeling photocurrent action spectra of photovoltaic devices based on organic thin films. J. Appl. Phys. *86*, 487-496.

53. Chen, K.-S., Salinas, J.-F., Yip, H.-L., Huo, L., Hou, J., and Jen, A.K.Y. (2012). Semi-transparent polymer solar cells with 6% PCE, 25% average visible transmittance and a color rendering index close to 100 for power generating window applications. Energy Environ. Sci. *5*, 9551-9557.

54. Yang, C., Liu, D., Bates, M., Barr, M.C., and Lunt, R.R. (2019). How to Accurately Report Transparent Solar Cells. Joule *3*, 1803-1809.